

Glioblastoma-instructed microglia transition to heterogeneous phenotypic states with phagocytic and dendritic cell-like features in patient tumors and patient-derived orthotopic xenografts

Yahaya A. Yabo^{1,2}, Pilar M. Moreno-Sanchez^{1,2}, Yolanda Pires-Afonso^{2,3}, Tony Kaoma⁴, Bakhtiyor Nosirov^{1,5}, Andrea Scafidi^{2,3}, Luca Ermini¹, Anuja Lipsa¹, Anaïs Oudin¹, Dimitrios Kyriakis^{2,6}, Kamil Grzyb⁶, Suresh K. Poovathingal^{6,7}, Aurélie Poli³, Arnaud Muller⁴, Reka Toth^{4,5}, Barbara Klink^{8,9,10,11}, Guy Berchem^{2,9,12}, Christophe Berthold¹², Frank Hertel¹², Michel Mittelbronn^{2,6,9,13,14}, Dieter H. Heiland^{15,16,17,18,19}, Alexander Skupin^{6,20,21}, Petr V. Nazarov^{4,5}, Simone P. Niclou^{1,2}, Alessandro Michelucci^{1,3,6,#}, Anna Golebiewska^{1,#}

¹NORLUX Neuro-Oncology Laboratory, Department of Cancer Research, Luxembourg Institute of Health (LIH), L-1526 Luxembourg, Luxembourg; ²Department of Life Sciences and Medicine, Faculty of Science, Technology and Medicine (FSTM), University of Luxembourg, L-4367 Belvaux, Luxembourg; ³Neuro-Immunology Group, Department of Cancer Research, Luxembourg Institute of Health, L-1526 Luxembourg, Luxembourg; ⁴Bioinformatics Platform, Department of Medical Informatics, Luxembourg Institute of Health, L-1445 Strassen, Luxembourg; ⁵Multomics Data Science, Department of Cancer Research, Luxembourg Institute of Health, L-1445 Strassen, Luxembourg; ⁶Luxembourg Centre for Systems Biomedicine (LCSB), University of Luxembourg, L-4362 Esch-sur-Alzette, Luxembourg; ⁷Single Cell Analytics & Microfluidics Core, Vlaams Instituut voor Biotechnologie-KU Leuven, 3000 Leuven, Belgium; ⁸National Center of Genetics, Laboratoire National de Santé, L-3555 Dudelange, Luxembourg; ⁹Department of Cancer Research, Luxembourg Institute of Health, L-1526 Luxembourg, Luxembourg; ¹⁰German Cancer Consortium (DKTK), 01307 Dresden, Germany; Core Unit for Molecular Tumor Diagnostics (CMTD), National Center for Tumor Diseases (NCT), 01307 Dresden, Germany; German Cancer Research Center (DKFZ), 69120 Heidelberg, Germany; ¹¹Institute for Clinical Genetics, Faculty of Medicine Carl Gustav Carus, Technische Universität Dresden, 01307 Dresden, Germany; ¹²Centre Hospitalier Luxembourg, 1210 Luxembourg, Luxembourg; ¹³Luxembourg Center of Neuropathology (LCNP), L-3555 Dudelange, Luxembourg; ¹⁴National Center of Pathology (NCP), Laboratoire National de Santé, L-3555 Dudelange, Luxembourg; ¹⁵Translational Neurosurgery, Friedrich-Alexander University Erlangen Nuremberg, 91054 Erlangen, Germany; ¹⁶Department of Neurosurgery, University Hospital Erlangen, Friedrich-Alexander University Erlangen Nuremberg, 91054 Erlangen, Germany; ¹⁷Department of Neurological Surgery, Northwestern University Feinberg School of Medicine, Chicago, IL 60611, USA; ¹⁸Department of Neurosurgery, Medical Center – University of Freiburg, 79106 Freiburg, Germany; ¹⁹German Cancer Consortium (DKTK), partner site Freiburg, 79106 Freiburg, Germany; ²⁰Department of Physics and Material Science, University Luxembourg, L-4367 Belvaux, Luxembourg; ²¹Department of Neuroscience, University of California San Diego, La Jolla, CA 92093, USA

Equal contribution; Correspondence: Anna.Golebiewska@lih.lu; Alessandro.Michelucci@lih.lu

SUPPLEMENTARY METHODS

Molecular profiling of PDOX models

Our current cohort comprises 46 glioma PDOX models. 39 PDOX models were characterized at the genetic and epigenetic levels. Targeted sequencing, copy number aberrations and DNA methylation profiling of PDOX models were performed as previously described [1] unless specified otherwise below.

Targeted DNA sequencing

500ng of extracted gDNA were diluted in 130µl low TE buffer (Qiagen) and sheared via sonication on a Bioruptor® UCD-200 (Diagenode) to an average fragment size of 150-300 bp DNA fragment size was determined using the DNA 1000 Kit on the Bioanalyzer 2100 (Agilent Technologies). A custom-made Agilent SureSelect^{XT} Target Enrichment Library (Cat No. G9612B) was used for Illumina Paired-End Multiplexed Sequencing on a MiSeq® instrument (Illumina). The panel design called panel 1 for the Target Enrichment Library was fully adapted from [2]. After design changes that were made using SureDesign - Agilent eArray (Agilent Technologies) we refer to it as panel 2 containing additional regions. Samples have been sequenced with version 1 of the panel or with version 2 of the panel (additional 53 genes). Library preparation was performed according to manufacturers' instructions. The Illumina MiSeq® Reagent Kit v3 (Cat No. MS-102-3003) was selected by applying the Illumina reagent selection algorithm.

Bioinformatics analysis of sequencing reads was performed using a Snakemake-based workflow [3], in accordance with GATK best practices. Briefly paired-end reads from each tumor were quality trimmed with fastp (v. 0.23.2) [4] and aligned to an *In silico* Combined human-mouse Reference Genome (ICRG) for mouse read cleaning using BWA mem (v. 0.7.17) [5] with default parameters. ICRG contained both the mouse (GRCm39) and human (Grch38/hg38) reference genomes. Reads mapping to human chromosomes were extracted from the resulting bam file using SAMtools (v. 1.17) and realigned only to the human reference genome with BWA mem. Duplicates were annotated with MarkDuplicates in GATK4 (v. 4.2.6.1). Base quality score recalibration was carried out in GATK4 using BaseRecalibrator and ApplyBQSR. Mosdepth was used to evaluate bam statistics [6]. MuTect2 (GATK4) was used in a tumor-only mode to identify somatic single nucleotide variants (SNVs) and short insertions and/or deletions (indels). To distinguish between germline and somatic variants, a hg38 GATK Panel of Normals was used. LearnReadOrientationModel (GATK4) was used to evaluate read orientation artefacts, while GetPileupSummaries (GATK4) and CalculateContamination (GATK4) were adopted to determine the proportion of contaminated reads across samples. The following criteria were used to identify variants: a minimum base quality score of 25, a minimum allele frequency of 5%, and a minimum 10X coverage. Variants caused by cross-sample contamination and read orientation artefacts were eliminated. The Ensembl Variant Effect Predictor (VEP) [7] was used to annotate somatic variants. Only variants identified by VEP as having a high or moderate impact were kept. Variants occurring in non-glioma specific genes were filtered out. Glioma specific genes: *IDH1*, *ATRX*, *TP53*, *CDKN2A*, *CDKN2B*, *EGFR*, *CDK4*, *CDK6*, *MDM2*, *MDM4*, *MET*, *MYCN*, *PDGFRA*, *NF1*, *PIK3CA*, *PIK3R1*, *PTCH1*, *PTEN*, *RB1*, *RET*, *STAG2*. Multiple genomic alterations were visualized with ComplexHeatmap [8] within R version 4.2.0.

DNA methylation

Methylation arrays with Infinium® MethylationEPIC were analysed as previously described [1] to establish the *MGMT* methylation and glioma classification by referencing data to the Molecular Neuropathology dataset [9].

10XGenomics single-cell RNA-sequencing and analysis

Human tumor cells were processed via Drop-seq (P3, P8, P13, T101, T16) or 10XGenomics (T192, T233, T347, T470). Drop-seq and data preprocessing were performed as previously described [1, 10]. For the 10XGenomics, purified single tumor cells were diluted to 10⁶ cells/ml with RNase free DPBS + 0.05 % FBS. Diluted cells were filtered using a 50µm filter. The viability of cells was verified using Beckman coulter automatic cell counter and C-Chip – Disposable Haemocytometer (NanoEntek) viability analyzer. Cell concentration was adjusted to target the encapsulation of 3000

cells according to 10XGenomics cell preparation guidelines. Chromium Next GEM Chip with single-cell suspension was loaded to the Chromium Controller (10XGenomics) for generation of encapsulated cells and GEMs. scRNA-seq libraries were prepared using the Chromium Next GEM Single Cell 3' GEM, Library & Gel Bead Kit v3.1 and a Chromium i7 Multiplex kit according to the manufacturer's protocol. Libraries were purified using SPRIselect magnetic beads and analyzed using Agilent 2100 Bioanalyzer. Sequencing was performed using NextSeq 500/550 High Output Kit v2.5 (75 Cycles). scRNA-seq analysis was performed in R (v4.1.1) with the Seurat package (v4.0.5) [11]. Barcode processing and UMI filtering were performed using the Cell Ranger 4.0.0. Average saturation of the sequencing was 30-40% as calculated by Cell Ranger. GBM molecular subtypes (Classical, Proneural and Mesenchymal) and cellular states (MES, AC, NPC and OPC-like) were determined using signatures listed in Wang et al., 2017 [12] and Neftel et al., 2019 [13] respectively. Single-cell signature scores were calculated using scrabble(v1.0.0) used in Neftel et al., 2019 [13].

Gene expression analysis by qPCR

Myelin was removed prior FACS-sorting with the Myelin removal beads II (Miltenyi) and CD11b⁺ cells were FACS-sorted directly to Trizol® LS (Life Technologies) according to the manufacturer's protocol (n=2-3; from at least 3 animals each). RNA extraction and RT-PCR were conducted as previously described [14]. The sequences of the primers designed with the Primer-BLAST tool are as follows: *Spp1* F: CTGGCTGAATTCTGAGGGACT, R: TTCTGTGGCGCAAGGAGATT; *P2ry12* F: GTGCAAGGGGTGGCATCTA, R: TGGAAGTTGCAGACTGGCAT; *Tmem119* F: TGCAATGTCGCTGTCACTCT, R: AGTTTGTGTTCCACGGGGT; *Grp34* F: GGAAAGCTTCAACTCAGTTCCTG, R: TCCATGAGAGGAGCAAAGCC; *Rpl27* F: ACATTGACGATGGCACCTC, R: GCTTGGCGATCTTCTTCTTG

SUPPLEMENTARY FIGURES

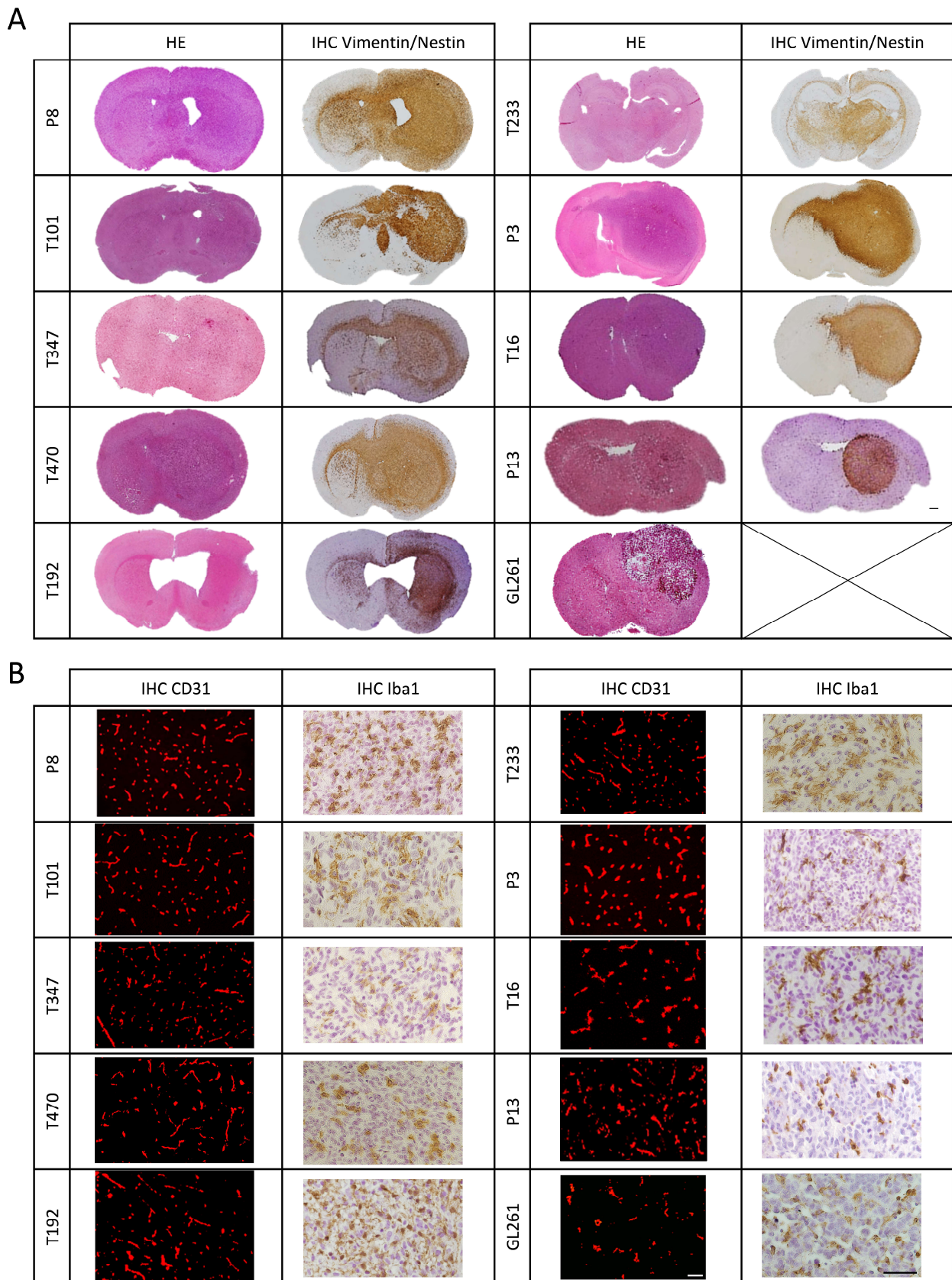


Fig S1. Characteristics of GBM PDOX models and the GL261 mouse model. (A) Hematoxylin and Eosin (H&E) and human-specific Vimentin/Nestin staining of representative PDOXs and GL261

at the endpoint of tumor growth. Human-specific Vimentin/Nestin staining highlights varying levels of invasion in PDOX models. Images represent coronal sections of the entire mouse brains. Mice were sacrificed at the endpoint of tumor growth. Scale bars represent 1mm. **(B)** Mouse-specific CD31 and Iba1 stainings show aberrant blood vessels and myeloid cells respectively. Brains of representative PDOXs and GL261 at the endpoint of tumor growth were used for the stainings. Images represent magnified areas in the tumor core. Hematoxylin staining was applied to assess tumor cell density. Scale bars represent 100µm (white) and 50µm (black).

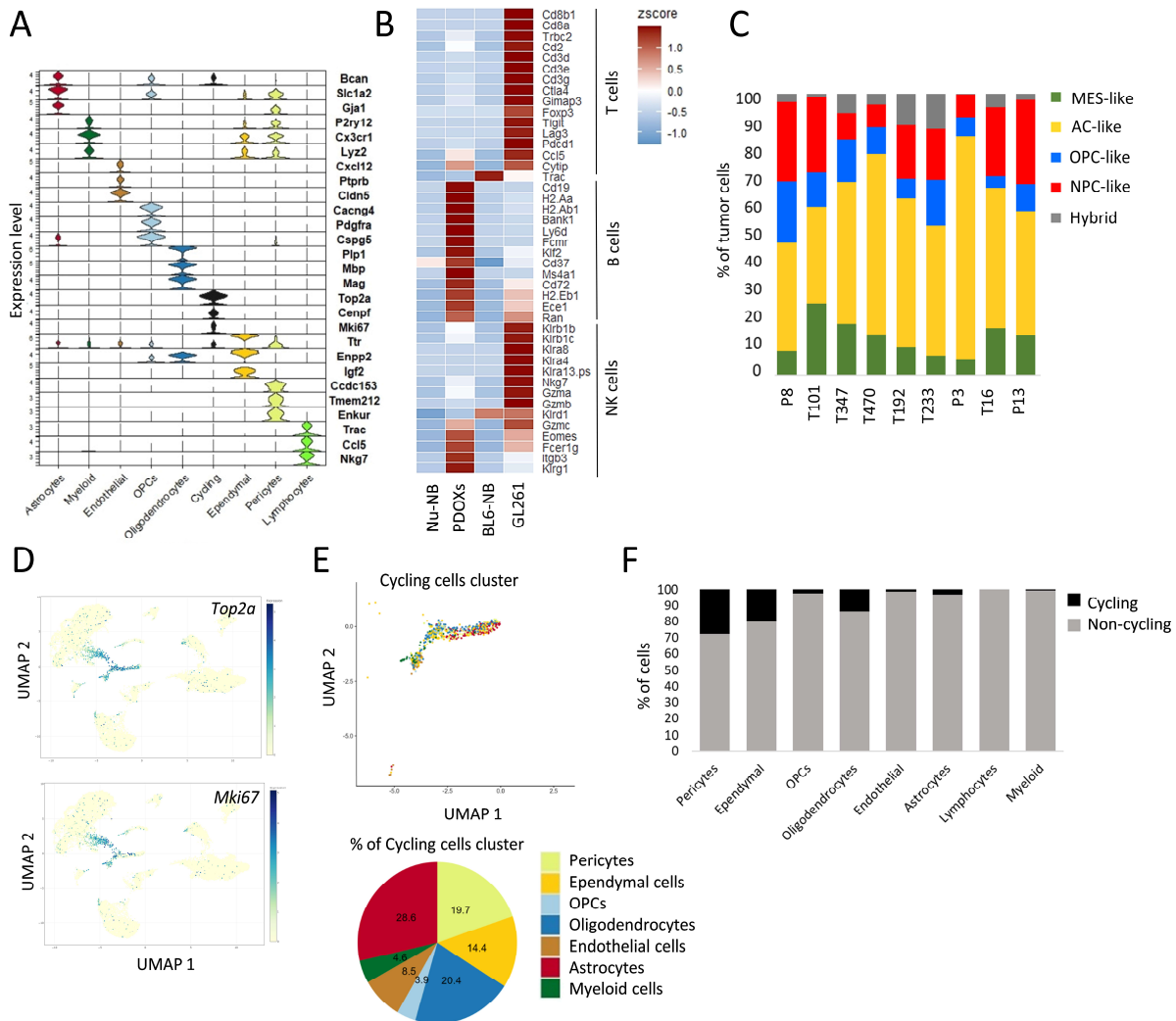


Fig S2. Composition of mouse-derived TME in PDOXs and GL261. **(A)** Violin plots showing expression of marker genes specific to distinct cell types identified in the scRNA-seq dataset. Three top markers of each population are displayed (Wilcoxon Rank Sum Test). For entire gene list see **Additional file 1: Table S3**. **(B)** Analysis of the lymphocyte cell cluster in nude mouse normal brain (Nu-NB), PDOXs (9 models), C57BL6/N mouse normal brain (BL6-NB), and GL261 tumor (3 collection time points: early, middle, and late). Heatmap shows the z-score of the average expression of marker genes for T, B and NK cells in lymphocytes detected in each sample group. **(C)** Human tumor cells of PDOX models assigned to four GBM transcriptomic states [13]: mesenchymal-like (MES-like), astrocytic-like (AC-like), oligodendrocyte progenitor cell-like (OPC-like) and neural progenitor cell-like (NPC-like). Cells with shared states were grouped as "Hybrid". **(D)** UMAPs showing expression of cell cycle marker genes *Top2a*, *Mki67* in TME. The color gradient represents expression levels. **(E)** Top: UMAP of the 'cycling cells' cluster and the proportion of cell types identified in the cluster. Cell types are color-coded. Bottom: proportions of identified cell types within the 'cycling cells' cluster. **(F)** Proportions of cycling cells in each cell type. 100% represents the sum

of cell numbers identified in each original cell type cluster and numbers of the same cell types identified in the ‘cycling cells’ cluster.

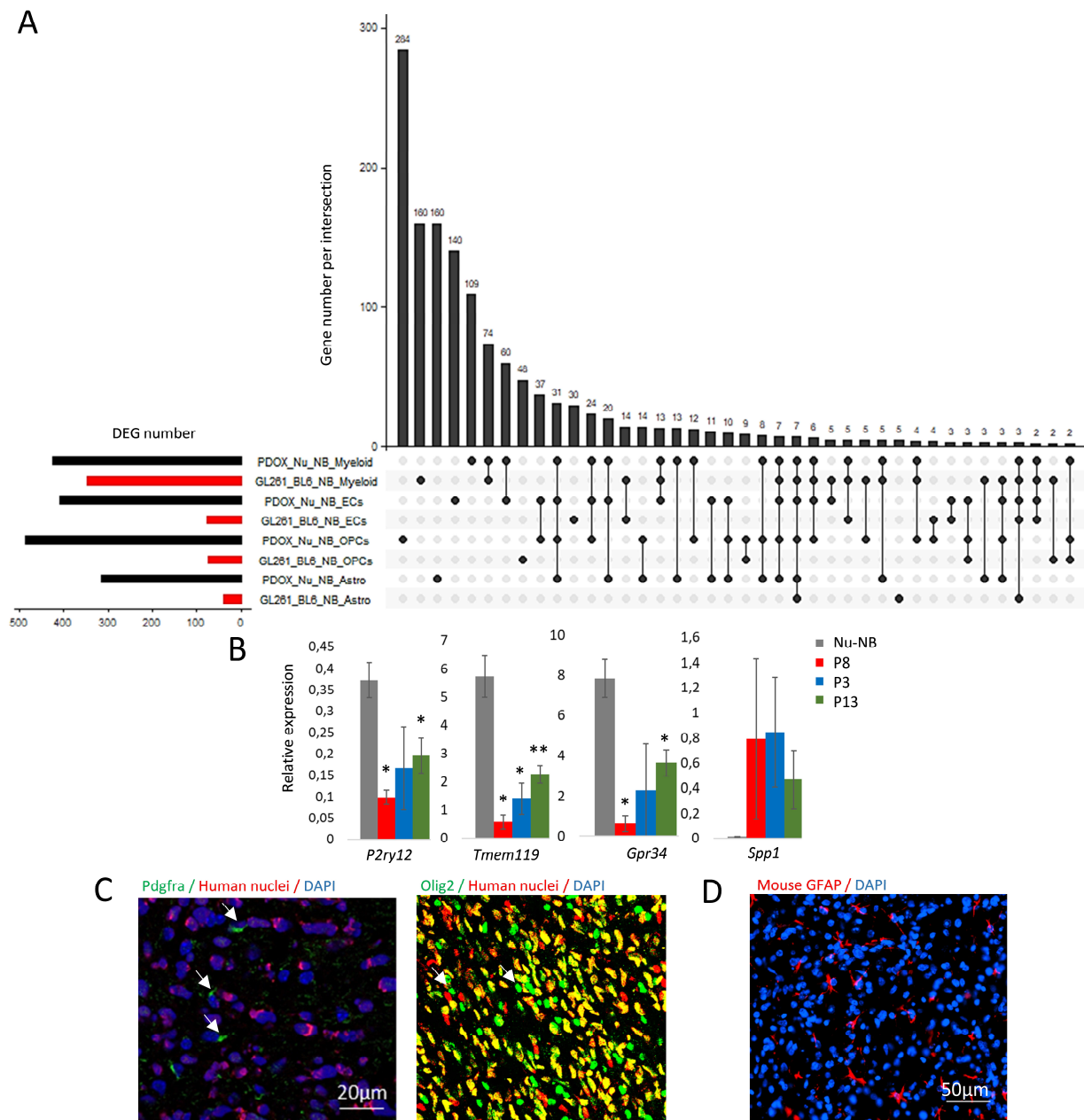


Fig S3. Tumor-specific activation of TME cell types. (A) Upset plot showing differentially expressed genes (DEGs) between TME of PDOX and GL261 versus corresponding normal brains (Nu-NB and BL6-NB) in identified cell types (FDR ≤ 0.01 , $|\log_2FC| \geq 1$, Wilcoxon rank sum test with Benjamini-Hochberg correction). Bar chart depicts the number of differentially expressed genes shared between the different groups. **(B)** Decreased expression of homeostatic Mg markers (*P2ry12*, *Tmem119*, *Gpr34*) and increased levels of a TAM marker (*Spp1*) were validated by qPCR in CD11b⁺ myeloid cells isolated as bulk from TME of representative PDOX models (P3, P8, P13) and nude normal brain (Nu-NB); graphs show bulk mean relative expression levels \pm SEM (n=2-5, **p<0.01 *p<0.05, two-tailed Student's t-test). *Rpl27* was used as a housekeeping gene. **(C)** Immunofluorescence staining showing Pdgfra⁺ and Olig2⁺ cells in the tumor core of PDOX P8. Arrows point Pdgfra⁺ and Olig2⁺ mouse cells, negative for human nuclei staining. **(D)** Immunofluorescence staining showing mouse GFAP⁺ astrocytic cells in the tumor core of PDOX T192.

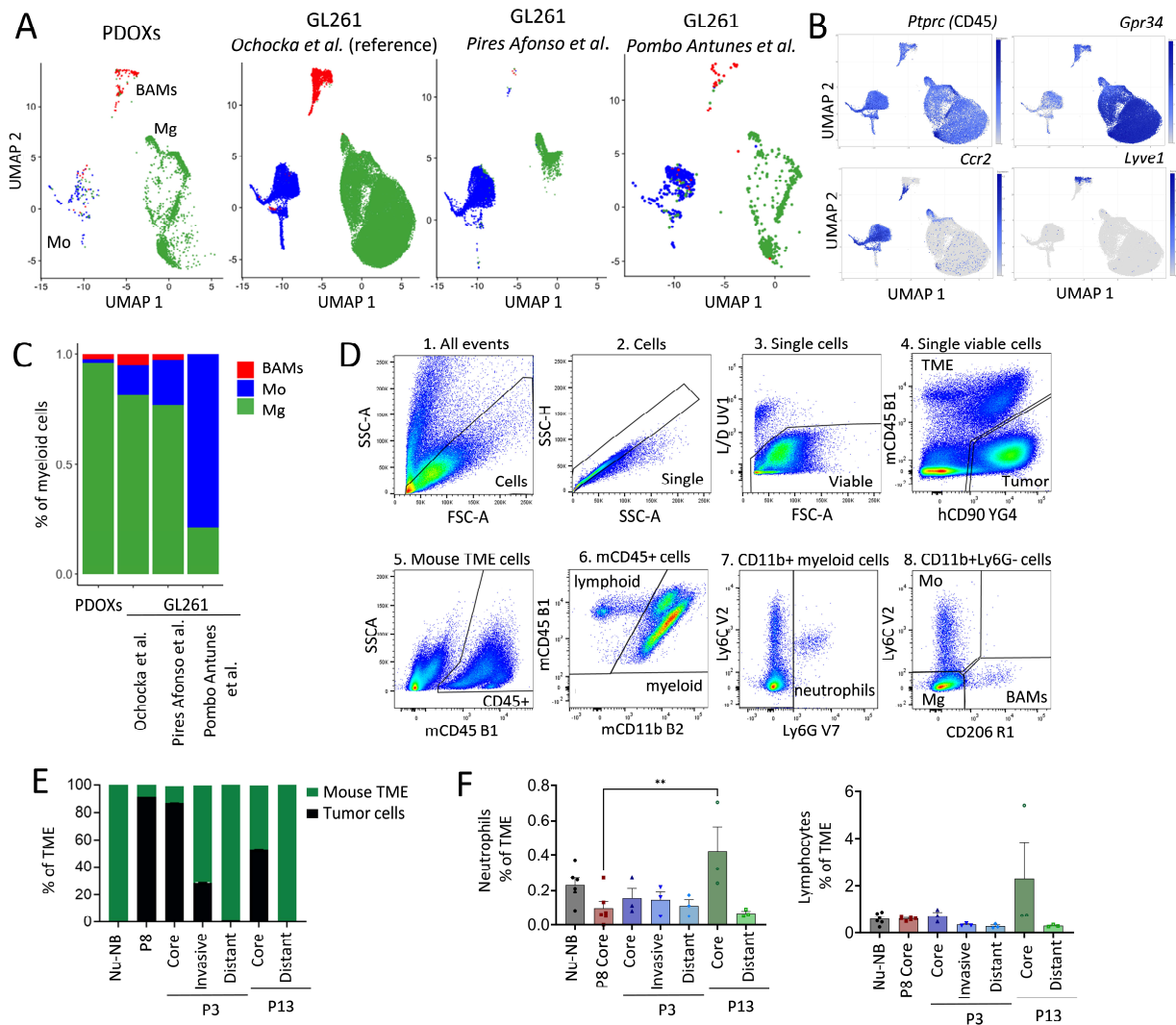


Fig S4. Myeloid cell heterogeneity and ontogeny in mouse-derived GBM TME. (A) Split UMAP projection of myeloid cells from different datasets. Myeloid cell types are color-coded (Mg = green, Mo = blue, BAMS = red). **(B)** UMAPs showing expression of marker genes: pan-immune *Ptprc* (CD45), Mg *Gpr34*, monocytes *Ccr2*, BAMS *Lyve1*. The color gradient represents expression levels. **(C)** Proportions of myeloid cell types in PDOXs and GL261 for three independent datasets [10, 15, 16]. Percentage of Mo depends on the tumor stage and dissection strategy. **(D)** Gating strategy for flow cytometry. Example is shown for PDOX P13 tumor: (1) Cells were distinguished from debris based on the Forward Scatter (FSC) and Side Scatter (SSC). (2) Cell aggregates were gated out based on their properties displayed on the SSC area (SSC-A) versus height (SSC-H) dot plot. (3) Dead cells were recognized by their strong positivity for the dead cell marker (L/D) (4) Human tumor cells were recognized as CD90 positive with human-specific antibody. TME was of mouse origin. (5) Immune cells were recognized as CD45 positive within mouse-derived TME. (6) Lymphocytes were recognized as CD11b negative population. Negative gating includes also CD11b^{low} NK cells. CD11b positive cells correspond to myeloid cells. (7) CD11b⁺Ly6C^{low}Ly6G⁺ cells represent neutrophils. (8) Ly6C and CD206 allows distinguishing Ly6C⁺CD206⁻ Mo, Ly6C⁻CD206⁻ Mg and Ly6C⁻CD206⁺ BAMS. **(E)** Ratio of human tumor cells over mouse-derived TME across distinct brain areas in PDOXs P8, P3 and P13 (≥3 mice/condition, mean ± SEM). The ratio of tumor cells to TME was higher in the tumor core compared to invasive zone and distal brain regions. **(F)** Flow cytometry quantification of CD45⁺CD11b⁺Ly6G⁺Ly6C^{low}CD206⁻ neutrophils and CD45⁺CD11b⁻ lymphocytes in Nu-NB and PDOX TME across different brain regions in PDOXs P3, P8 and P13 (n≥3 mice/condition, mean ± SEM, one-way ANOVA, **p<0.01).

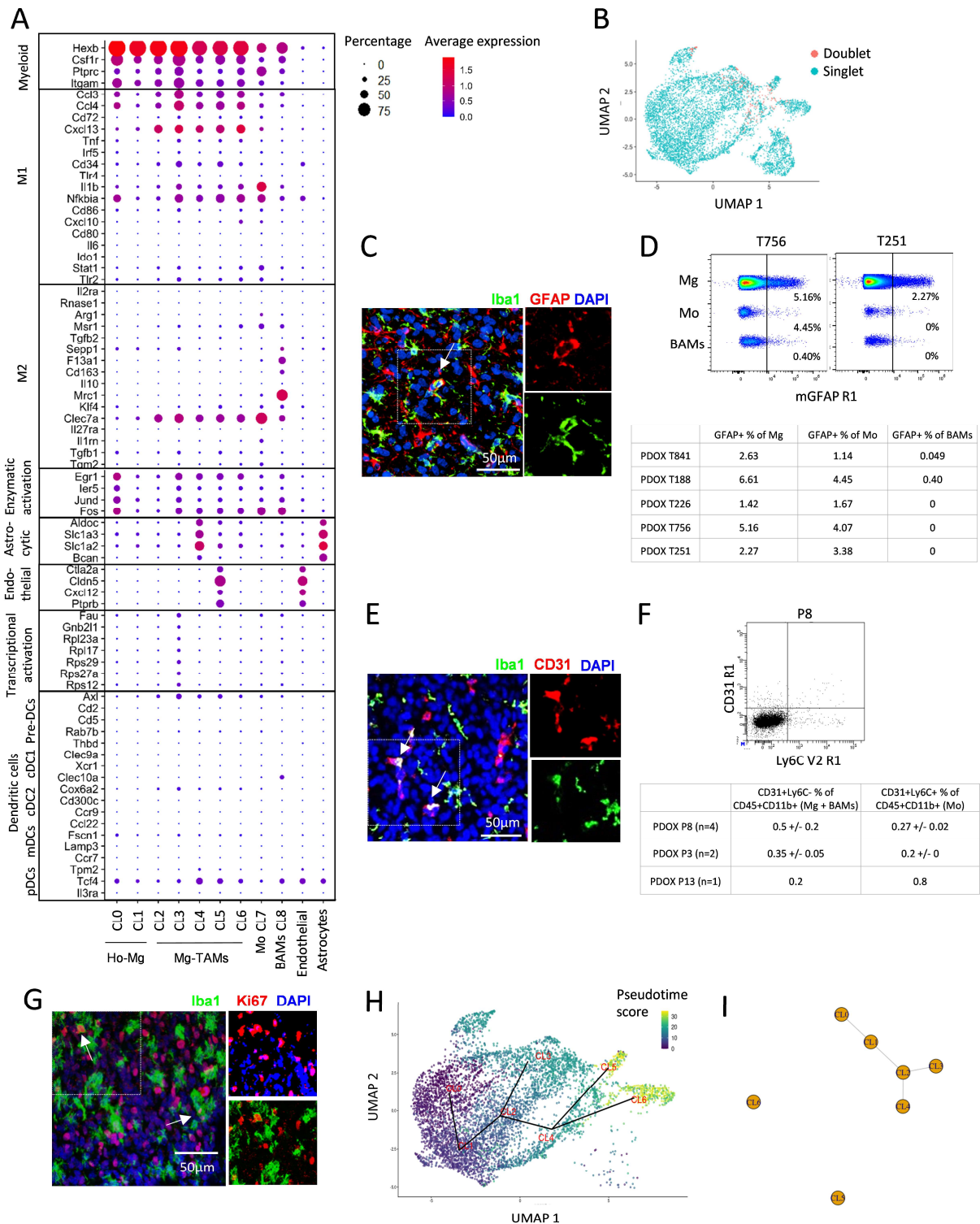


Fig S5. Analysis of heterogeneous myeloid phenotypic states. (A) Expression levels of exemplary genes representing myeloid pan-markers, M1/M2 markers, enzymatic activation genes, astrocytic and endothelial Mg-TAM markers, transcriptional activation markers and key markers identifying distinct subsets of dendritic cells (DCs): pre-DCs, cDC1, cDC2, migratory DCs (mDCs) and pDCs per identified myeloid cell cluster: CL0-1 Ho-Mg, CL2-6 Mg-TAMs, CL7 Mo, CL8 BAMs. Astrocytes and endothelial cells were presented to compare marker genes identified in CL4 astrocytic-like and CL5 endothelial-like Mg-TAMs. (B) Scoring for putative doublets in the myeloid cells. (C) Representative immunofluorescence images showing mouse Iba1⁺ myeloid cells positive for GFAP (astrocytic marker, PDOX T192), White arrow point GFAP⁺Iba1⁺ co-localization. Scale bar

represents 50 μ m. **(D)** Flow cytometry assessment of GFAP positivity in Mg, Mo and BAMs. Flow cytometry example is shown for PDOX T756 and T251. Table displays % of GFAP⁺ cells in each PDOX assessed; n=1 mouse/model. **(E)** Representative immunofluorescence images showing mouse Iba1⁺ myeloid cells positive for CD31 (endothelial marker, PDOX T470). White arrows point CD31⁺Iba1⁺ co-localization. Scale bar represents 50 μ m. **(F)** Flow cytometry assessment of CD31 positivity in CD45⁺CD11b⁺ myeloid cells discriminated by Ly6C (Ly6C⁻ Mg and BAMs; Ly6C⁺ Mo). Flow cytometry example is shown for PDOX P3. Table displays % of CD31⁺ cells in each PDOX assessed; mean \pm SEM, n=1-4 mice/condition. **(G)** Representative immunofluorescence images showing mouse Iba1⁺ myeloid cells positive for Ki67 (cell cycle marker, PDOX P8). White arrows point Ki67⁺Iba1⁺ co-localization. Scale bar represents 50 μ m. **(H)** TSCAN-based trajectory inference analysis of Mg clusters (CL0-6) showing a trajectory from Ho-Mg to Mg-TAMs. The Pseudotime ordering of cells is presented by a color code on the original UMAP projection. **(I)** Minimum spanning tree (MST) of the Mg clusters after introducing an outgroup to split unrelated trajectories.

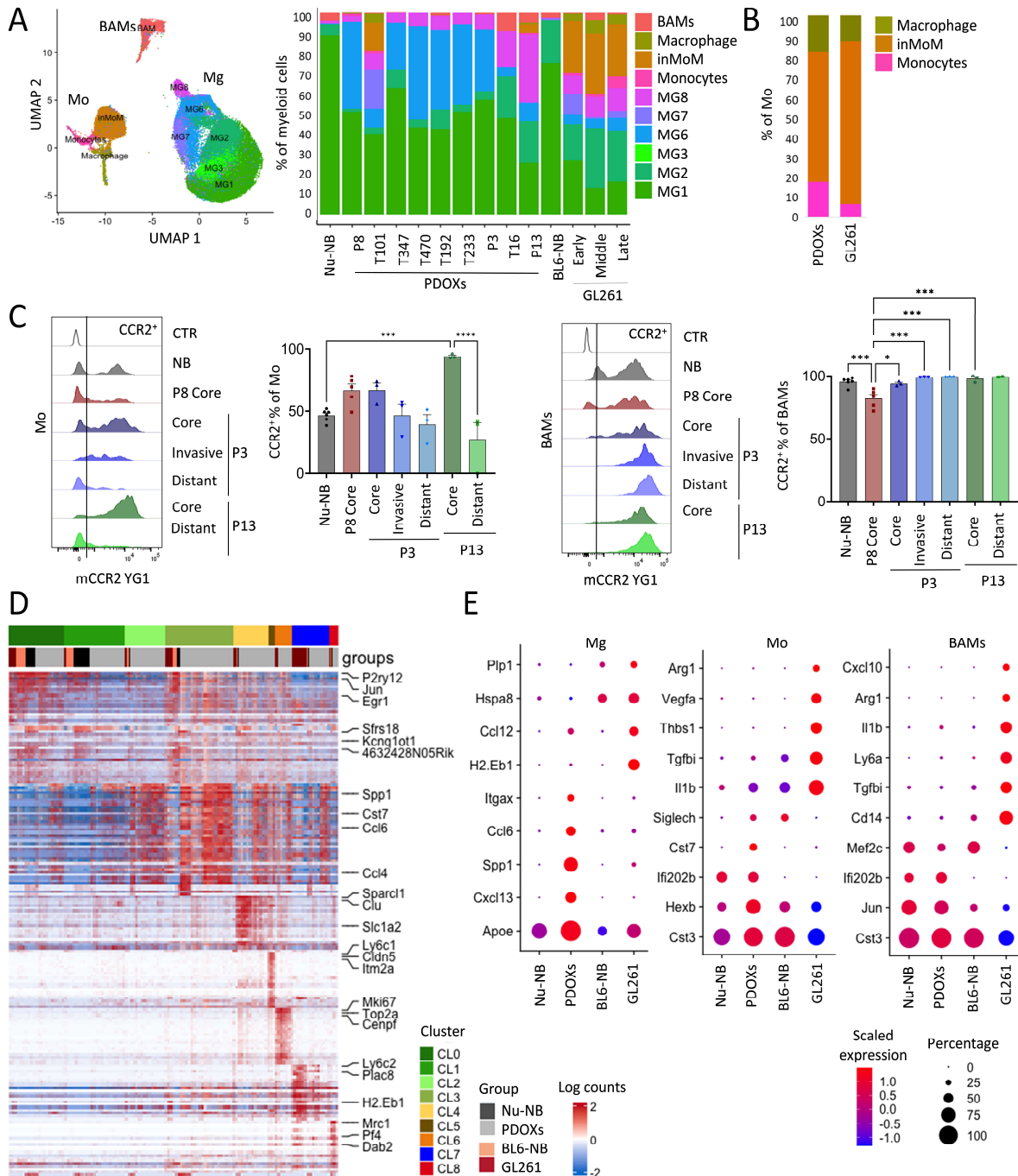


Fig S6. GBM-specific education of myeloid cells in PDOXs and GL261 TME. (A) Reference-based analysis of myeloid cell states described by Ochocka et al., in PDOXs and GL261: (i) MG1-MG8 states correspond to Mg, (ii) Monocyte, Intermediate Monocytes/Macrophage (inMoM) and Macrophage states correspond to Mo, no further phenotypic states were identified for BAMs. **(B)** Proportions of phenotypic states identified by reference-based analysis in Mo in PDOXs (4 models with Mo cells detected combined) and GL261 (3 time points combined). **(C)** Representative flow cytometry graphs and quantification of CCR2⁺ cells in CD45⁺CD11b⁺Ly6G⁻Ly6C⁺CD206⁻ Mo and CD45⁺CD11b⁺Ly6G⁻Ly6C⁻CD206⁺ BAMS in PDOXs P8, P3, P13. For PDOXs P3 and P13 invasive zone and distant normal brain areas were also collected (n≥3 mice/condition, mean ± SEM, one-way ANOVA, ****p<0.0001, ***p<0.001, *p<0.05). **(D)** Comparison of transcriptomic profiles of myeloid cells in PDOXs and GL261 models. Heatmap represents expression of marker genes of each myeloid transcriptomic state identified (CL0-8). No major differences were observed between myeloid cells of PDOXs and GL261. **(E)** Expression levels of representative genes in Mg, Mo and BAMS for nude mouse normal brain (Nu-NB), PDOXs (9 models), C57BL6/N mouse normal brain (BL6-NB), GL261 tumor (3 collection time points: early, middle, and late).

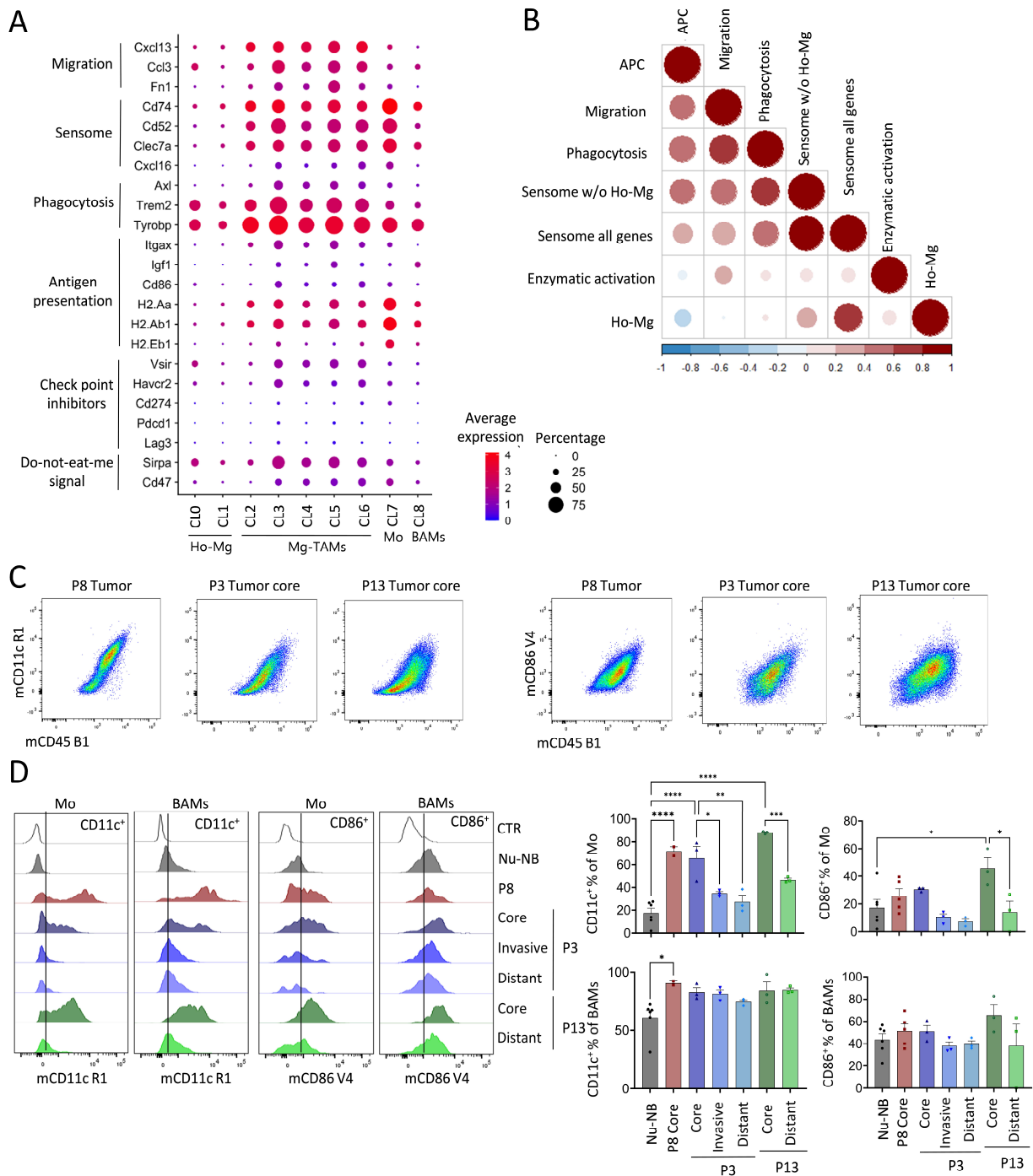


Fig S7. Analysis of functional markers in TAMs. (A) Expression levels of representative genes associated with functional signatures for migration, sensome (GBM specific), phagocytosis, antigen presentation, checkpoint inhibition and “do-not-eat-me signal” per identified myeloid cell cluster: CL0-1 Ho-Mg, CL2-6 Mg-TAMs, CL7 Mo, CL8 BAMs. **(B)** Spearman correlation analysis between functional signatures in myeloid cells. **(C)** Representative flow cytometry graphs showing high levels of CD11c and CD86 with CD45^{high} Mg. Mg was gated as CD45⁺CD11b⁺Ly6G⁻Ly6C⁻CD206⁻ **(D)** Representative flow cytometry graphs and quantification of CD11c⁺ and CD86⁺ cells in CD45⁺CD11b⁺Ly6G⁻Ly6C⁻CD206⁻ Mo and CD45⁺CD11b⁺Ly6G⁻Ly6C⁻CD206⁻ BAMs in nude mouse normal brain (Nu-NB) and PDOXs P8, P3, P13. For PDOXs P3 and P13 invasive zone and distant normal brain areas were also collected. Unstained control is shown for each population (CTR) (n≥3 mice/condition, mean ± SEM, one-way ANOVA, **0*p<0.0001, **p<0.01, *p<0.05).

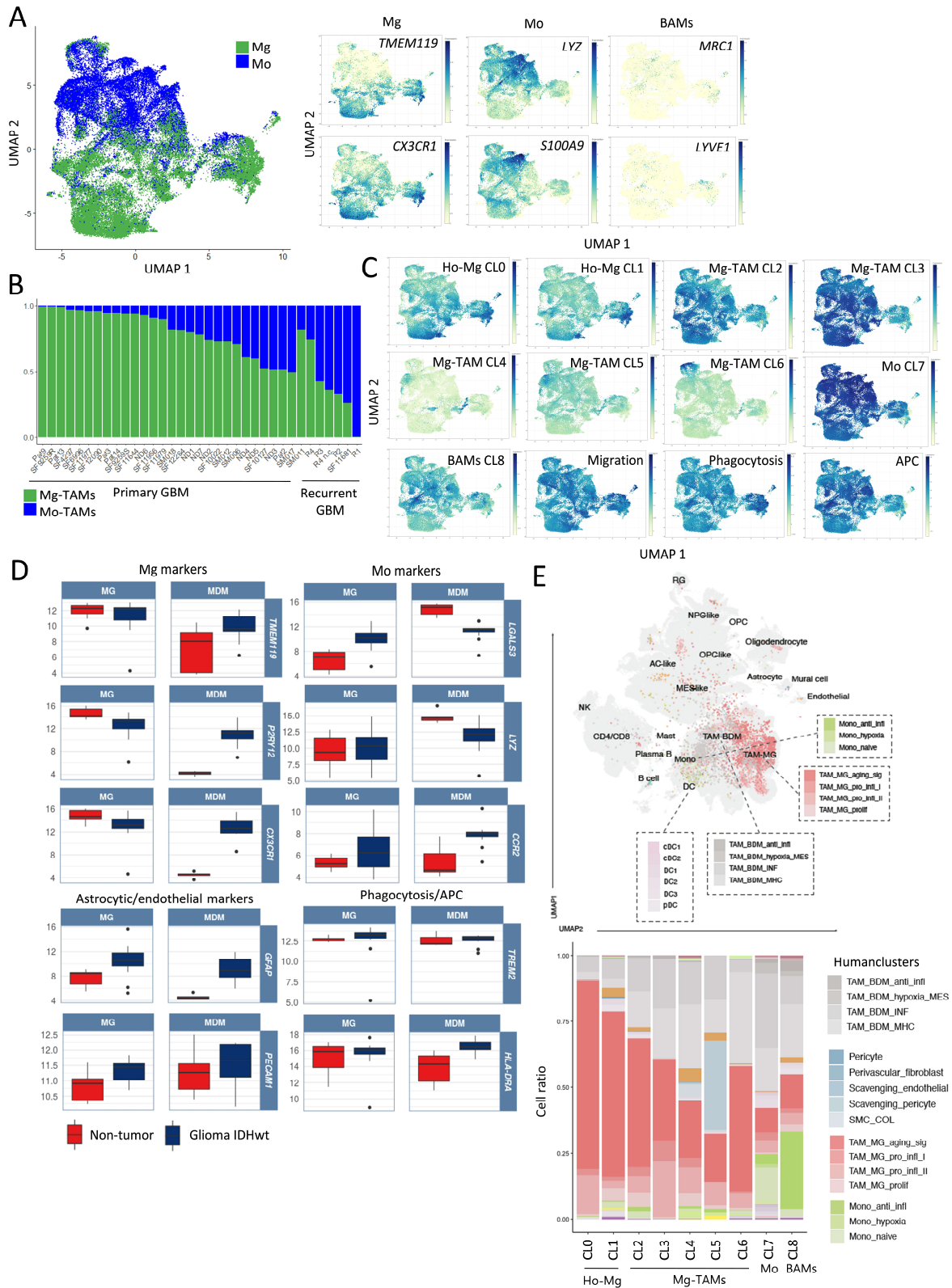


Fig S8. Analysis of Mg and Mo cells in GBM patient tumors. (A) UMAP projection of myeloid cells in GBM patient tumors (n=36 patients combined). Cells are color coded for Mg and Mo ontogeny based on established gene signatures. Inserts show expression levels of marker genes for Mg, Mo and BAMs. The color gradient represents expression levels. (B) Proportions of Mg and Mo in individual GBM patient tumors (36 patient tumors: 27 newly diagnosed and 9 recurrent tumors). Recurrent GBMs show higher proportions of Mo (p<0.01, two-tailed Student’s t-test). (C) UMAP projection of human GBM myeloid cells displaying expression levels of cluster (CL0-8) and functional

signatures identified in PDOX TME. The color gradient represents expression levels. **(D)** Expression of representative Mg, Mo, astrocyte and endothelial cell markers showing convergence of Mg and Mo towards heterogeneous TAMs in GBM tumors. Bulk RNA-seq analysis was performed in purified CD49d⁺ (MG) and CD49⁻ (MDM) myeloid cells [17] representing Mg and Mo in normal human brain (n=7) and GBM patient tumors (n=15). While Mg decreases homeostatic genes, Mo acquire Mg profiles within GBM tumors. Reversed convergence is observed for Mo markers. **(E)** Mapping of mouse myeloid cells to the scRNA-seq profiles of human GBMs (110 patient tumors, GBmap [18]). Mg states (CL0-CL6) predominantly mapped to previously identified human Mg states, although Mg-TAMs (CL3, CL4, CL6) showed increased proportion of TAMs associated with blood-derived macrophages (BDMs), highlighting strong convergence of the Mg and Mo towards comparable TAM signatures. The astrocytic-like CL4 state is clearly associated with human myeloid compartment, whereas the endothelial-like CL5 state only partially overlapped with pericytes and endothelial cells. Mo (CL7) and BAMs (CL8) showed a stronger association with Mo signatures.

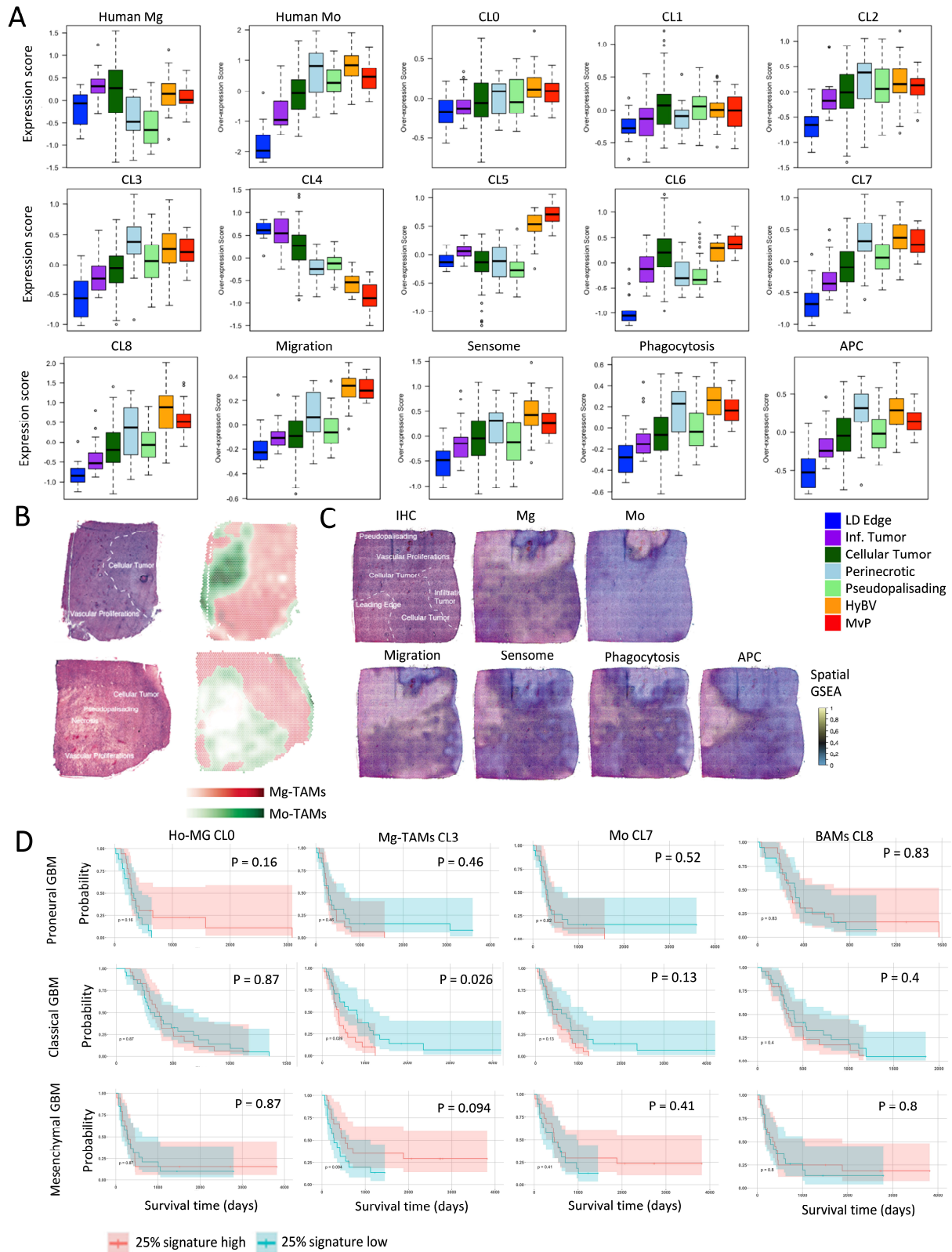


Fig S9. Assessment of myeloid signatures in bulk RNA-seq profiles of GBM patient tumors. (A) Bulk RNA-seq profiles of laser-micro dissected regions of GBM patient tumors. Box plots show signatures of Mg/Mo, phenotypic states and functional signatures per tumor niche (LD edge: leading edge; Inf tumor: infiltrative tumor; HyBV: hyperplastic blood vessels in cellular tumor; MvP: microvascular proliferation). Data extracted from the Ivy Glioblastoma Atlas Project obtained from 279 samples from 44 tumors. The box limits indicate the 25th and 75th percentiles, centerlines show

the medians; whiskers show a minimum of two measures: extreme values or 1.5 IQR from the closest quartile; points depict outliers. **(B-C)** Representative surface plots of spatial localization of myeloid cell signatures in GBM patient tumors. **(D)** Kaplan–Meier survival analysis in GBM patients (CGGA-GBM IDHwt divided into transcriptomic subtypes: Classical, Mesenchymal and Proneural) with high- (red) and low (blue) -enriched signatures (25 percentile top/bottom).

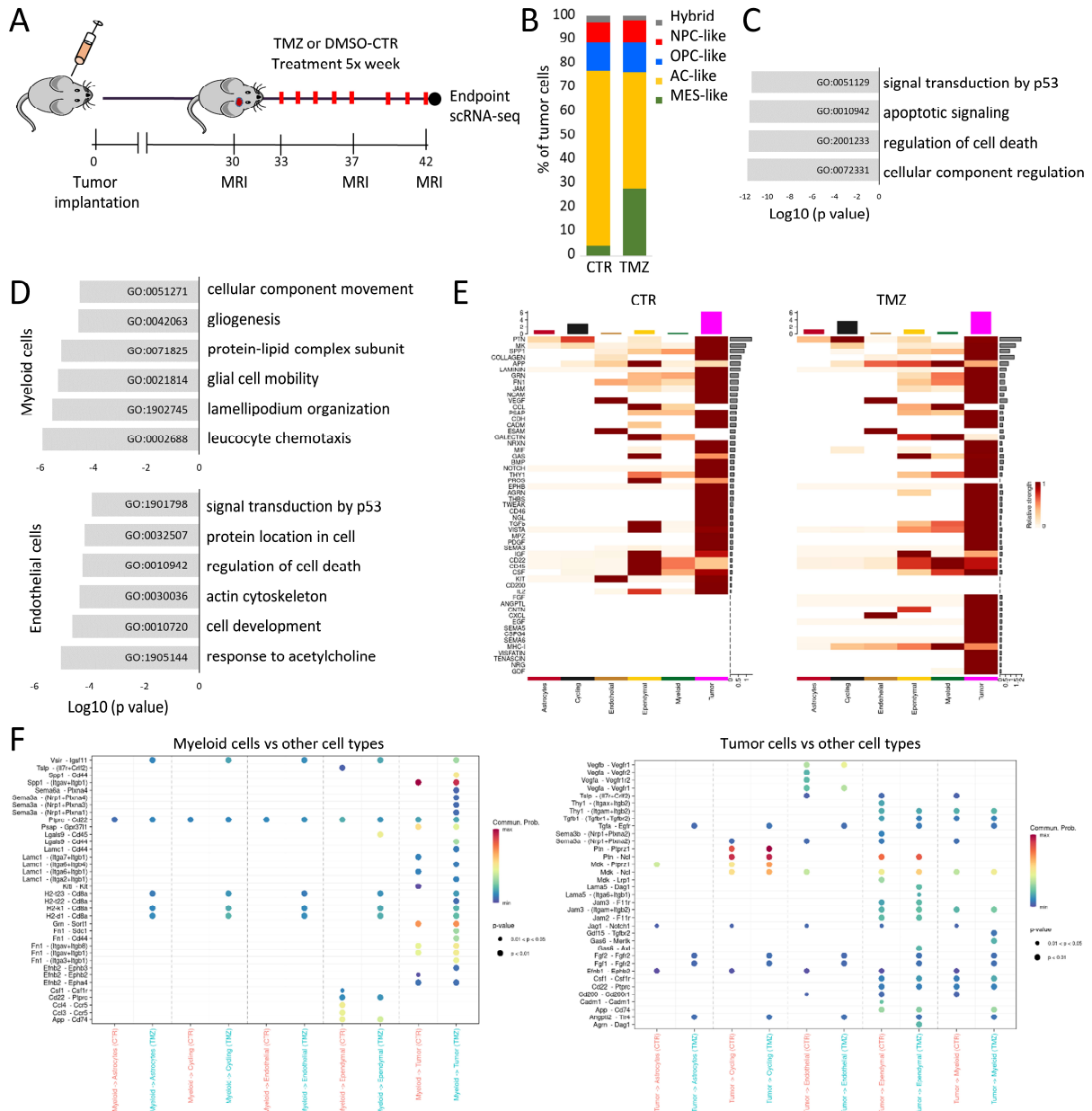


Fig S10. GBM ecosystem upon TMZ treatment. (A) Schematic illustration of the TMZ treatment regimen in PDOX P3 *in vivo*. Day 0 = tumor implantation, day 30 = MRI validation of tumor growth, day 33 = treatment start, day 37 = intermediary MRI, day 42 = endpoint. Created with Biorender.com. **(B)** Assessment of GBM cellular states [13] at single cell level in TMZ-treated and CTR GBM cells (n=1 PDOX brain per condition). **(C)** Summary of top four gene ontology terms characterizing DEGs in TMZ-treated versus CTR GBM cells (FDR ≤ 0.01, |logFC| ≥ 0.5 the Wilcoxon rank sum test with Benjamini-Hochberg correction). **(D)** Summary of top six gene ontology terms characterizing DEGs in TMZ-treated versus CTR myeloid and endothelial cells forming TME in PDOX P3 (FDR ≤ 0.01, |logFC| ≥ 0.5). **(E)** CellChat-based overall signaling patterns per identified cell type, visualized as heatmaps, in CTR and TMZ-treated PDOXs. **(F)** Predicted ligand-receptor interactions based on communication probability are shown for signals outgoing from myeloid and tumor cells.

SUPPLEMENTARY REFERENCES

1. Golebiewska, A., A.C. Hau, A. Oudin, D. Stieber, Y.A. Yabo, et al., *Patient-derived organoids and orthotopic xenografts of primary and recurrent gliomas represent relevant patient avatars for precision oncology*. Acta Neuropathol, 2020. **140**(6): p. 919-949.DOI: 10.1007/s00401-020-02226-7.
2. Sahm, F., D. Schrimpf, D.T. Jones, J. Meyer, A. Kratz, et al., *Next-generation sequencing in routine brain tumor diagnostics enables an integrated diagnosis and identifies actionable targets*. Acta Neuropathol, 2016. **131**(6): p. 903-10.DOI: 10.1007/s00401-015-1519-8.
3. Molder, F., K.P. Jablonski, B. Letcher, M.B. Hall, C.H. Tomkins-Tinch, et al., *Sustainable data analysis with Snakemake*. F1000Res, 2021. **10**: p. 33.DOI: 10.12688/f1000research.29032.2.
4. Chen, S., Y. Zhou, Y. Chen, and J. Gu, *fastp: an ultra-fast all-in-one FASTQ preprocessor*. Bioinformatics, 2018. **34**(17): p. i884-i890.DOI: 10.1093/bioinformatics/bty560.
5. Callari, M., A.S. Batra, R.N. Batra, S.J. Sammut, W. Greenwood, et al., *Computational approach to discriminate human and mouse sequences in patient-derived tumour xenografts*. BMC Genomics, 2018. **19**(1): p. 19.DOI: 10.1186/s12864-017-4414-y.
6. Pedersen, B.S. and A.R. Quinlan, *Mosdepth: quick coverage calculation for genomes and exomes*. Bioinformatics, 2018. **34**(5): p. 867-868.DOI: 10.1093/bioinformatics/btx699.
7. McLaren, W., L. Gil, S.E. Hunt, H.S. Riat, G.R. Ritchie, et al., *The Ensembl Variant Effect Predictor*. Genome Biol, 2016. **17**(1): p. 122.DOI: 10.1186/s13059-016-0974-4.
8. Gu, Z., R. Eils, and M. Schlesner, *Complex heatmaps reveal patterns and correlations in multidimensional genomic data*. Bioinformatics, 2016. **32**(18): p. 2847-9.DOI: 10.1093/bioinformatics/btw313.
9. DKFZ. *MolecularNeuropathology.org - The platform for next generation neuropathology*. 2023; Available from: <https://www.molecularneuropathology.org/mnp/>.
10. Pires-Afonso, Y., A. Muller, K. Grzyb, A. Oudin, Y.A. Yabo, et al., *Elucidating tumour-associated microglia/macrophage diversity along glioblastoma progression and under ACOD1 deficiency*. Mol Oncol, 2022. **16**(17): p. 3167-3191.DOI: 10.1002/1878-0261.13287.
11. Hao, Y., S. Hao, E. Andersen-Nissen, W.M. Mauck, 3rd, S. Zheng, et al., *Integrated analysis of multimodal single-cell data*. Cell, 2021. **184**(13): p. 3573-3587 e29.DOI: 10.1016/j.cell.2021.04.048.
12. Wang, Q., B. Hu, X. Hu, H. Kim, M. Squatrito, et al., *Tumor Evolution of Glioma-Intrinsic Gene Expression Subtypes Associates with Immunological Changes in the Microenvironment*. Cancer Cell, 2017. **32**(1): p. 42-56 e6.DOI: 10.1016/j.ccell.2017.06.003.
13. Neftel, C., J. Laffy, M.G. Filbin, T. Hara, M.E. Shore, et al., *An Integrative Model of Cellular States, Plasticity, and Genetics for Glioblastoma*. Cell, 2019. **178**(4): p. 835-849 e21.DOI: 10.1016/j.cell.2019.06.024.
14. Sousa, C., A. Golebiewska, S.K. Poovathingal, T. Kaoma, Y. Pires-Afonso, et al., *Single-cell transcriptomics reveals distinct inflammation-induced microglia signatures*. EMBO Rep, 2018.DOI: 10.15252/embr.201846171.
15. Pombo Antunes, A.R., I. Scheyltjens, F. Lodi, J. Messiaen, A. Antoranz, et al., *Single-cell profiling of myeloid cells in glioblastoma across species and disease stage reveals macrophage competition and specialization*. Nat Neurosci, 2021. **24**(4): p. 595-610.DOI: 10.1038/s41593-020-00789-y.
16. Ochocka, N., P. Segit, K.A. Walentynowicz, K. Wojnicki, S. Cyranowski, et al., *Single-cell RNA sequencing reveals functional heterogeneity of glioma-associated brain macrophages*. Nat Commun, 2021. **12**(1): p. 1151.DOI: 10.1038/s41467-021-21407-w.
17. Klemm, F., R.R. Maas, R.L. Bowman, M. Kornete, K. Soukup, et al., *Interrogation of the Microenvironmental Landscape in Brain Tumors Reveals Disease-Specific Alterations of Immune Cells*. Cell, 2020. **181**(7): p. 1643-1660 e17.DOI: 10.1016/j.cell.2020.05.007.
18. Ruiz-Moreno, C., S.M. Salas, E. Samuelsson, S. Brandner, M.E.G. Kranendonk, et al., *Harmonized single-cell landscape, intercellular crosstalk and tumor architecture of glioblastoma*. bioRxiv, 2022: p. 2022.08.27.505439.DOI: 10.1101/2022.08.27.505439.